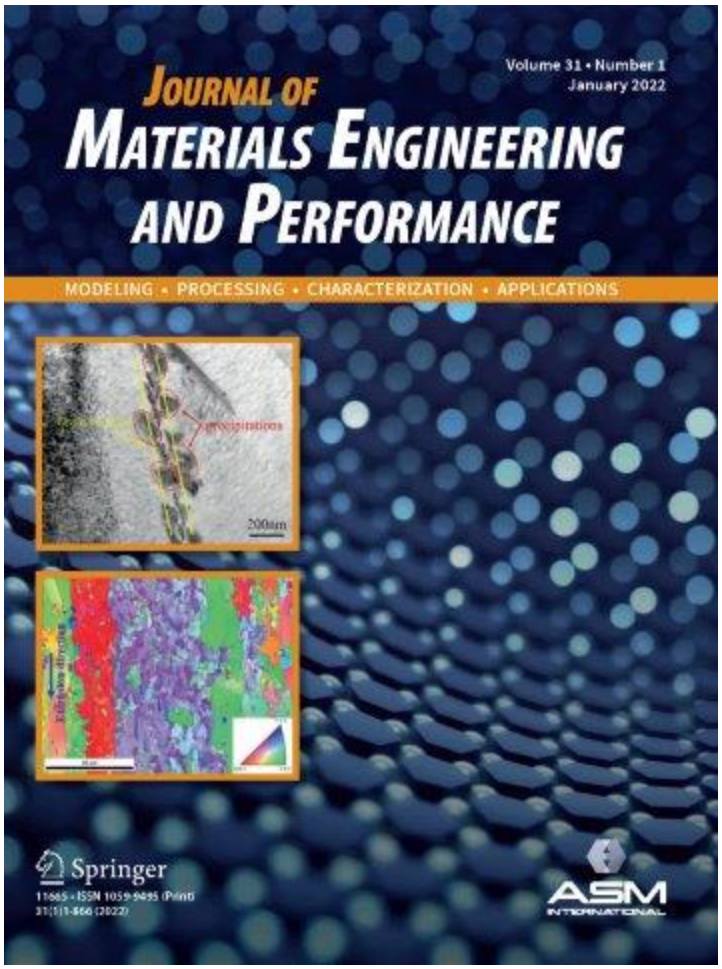

A probe into the corrosion behaviour of a WE43B magnesium alloy in a simulated body fluid using the dynamic-EIS

Journal:	*Journal of Materials Engineering and Performance*
Manuscript ID	JMEP-23-02-31217.R3
Manuscript Type:	Original Research Article
Date Submitted by the Author:	09-Oct-2023
Complete List of Authors:	Gerengi, Husnu; Duzce University, Department of Mechanical Engineering lorenzi , sergio; University of Bergamo, Department of Engineering and Applied Sciences Solomon, Moses; Covenant University, Chemistry Slepski, Pawel; Gdańsk University of Technology, Department of Electrochemistry, Corrosion and Materials Engineering Gratton, Sara; University of Bergamo, Department of Engineering and Applied Sciences

	Cabrini , Marina ; University of Bergamo, Department of Engineering
Keywords:	Biomedical implant, Corrosion in simulated body fluid, WE43B alloy, Dynamic-EIS

A probe into the corrosion behaviour of a WE43B magnesium alloy in a simulated body fluid using the dynamic-EIS

Husnu Gerengi[1,2], Sergio Lorenzi[2], Moses M. Solomon[3], Pawel Slepski[4], Sara Gratton[2] Marina Cabrini[2]

[1]Corrosion Research Laboratory, Department of Mechanical Engineering, Faculty of Engineering, Duzce University, 81620 Duzce, Turkey.
[2]Department of Engineering and Applied Sciences, University of Bergamo, 24044 Dalmine, BG, Italy.
[3]Department of Chemical and Environmental Engineering, University of Nottingham, Ningbo, China.
[4]Department of Electrochemistry, Corrosion and Materials Engineering, Faculty of Chemistry, Gdańsk University of Technology, Gdańsk 80-233, Poland.

Abstract

WE43B is one of the newest Mg alloys with practical application in biomedical implant technology. This work attempts to scrutinize the corrosion characteristics of WE43B alloy in a simulated body fluid (SBF) at a typical body temperature. The dynamic-electrochemical impedance spectroscopy (DEIS) with the capacity to track changes on surfaces in a dynamic corrosive system is used in combination with other classical techniques namely, linear polarization, EIS, and hydrogen evolution to track the corrosion pattern of the alloy in SBF for 24 h. The electrochemical results reveal a steady increase in the corrosion resistance of the alloy with immersion time reaching 1398 Ω cm^2 at 24 h. This corroborates the hydrogen evolution results in which a declining trend in the corrosion rate with immersion time is observed. The corrosion rate of the alloy is in the range of 1.326 – 1.338 mm y^{-1} at 24 h. The results from the applied techniques are comparable. The surface analysis (scanning electron microscope (SEM), energy-dispersive X-ray spectroscopy (EDX), atomic force microscopy AFM) results conform with the results obtained from applied methods.

Keywords: Biomedical implant; Corrosion in simulated body fluid; WE43B alloy; Dynamic-EIS.

1. Introduction

In recent times, there has been significant research interest in magnesium and its alloys for biomedical implant technology (Ref 1–7). The growing interest is due to the attractive properties of this metal which include the light weight (1.74 – 2.00 g/cm^3 which is close to the bone density of 1.80 – 2.00 g/cm^3), the comparable elastic modulus with that of a human bone, the excellent shock resistance, biodegradability, and biocompatibility (Ref 8–10). However, at present, few magnesium alloys have actually gained practical biomedical application. This is due to the ease at which Mg and its alloys lost the attractive properties to corrosion in the

physiological environment as well as the excessive evolution of hydrogen gas that could result in subcutaneous hydrogen accumulation in the body (Ref 11).

The corrosion resistance property of magnesium can be enhanced by alloying with other elements (Ref 12,13). It was noted that a step-by-step building of alloy systems to an optimum concentration of the alloying element(s) enhanced the corrosion resistance significantly (Ref 14). Bakhsheshi-Rad *et al*. (Ref 15) found that the corrosion resistance of Mg–0.5Ca alloy was enhanced with the addition of Zn up to 1%, while further addition reversed the effect. Beside alloying, other techniques such as heat treatment (Ref 15,16), coating (Ref 17,18), *etc*. Gül *et al*. (Ref 17,18) demonstrated that AZ91 Mg alloy coated with tantalum oxide is promising for biomedical applications because of its enhanced corrosion resistance. As earlier mentioned, the susceptibility of Mg and its alloys to corrosion in physiological system is one its undermining factor towards its full deployment in biomedical application, hence several research works have been performed in simulated physiological environments to better understand the corrosion mechanism and how to mitigate (Ref 19,20).

The AZ alloys group with Al and Zn as the main alloying elements have been widely studied for potential biomedical applications (Ref 1–7). The Al is intended to improve the alloy mechanical properties and ductility while its combination with Zn is expected to enhance the corrosion resistance property by eliminating the negative effect of other elements like Fe, Ni, etc. on the alloy corrosion resistance (Ref 12,13). However, the biocompatibility of these alloying elements especially Al has come under severe criticism with authors arguing that long term exposure to Al could affect reproductive ability (Ref 21), induce dementia (Ref 22), and could cause Alzheimer's disease (Ref 23,24). Conversely, Y and Nb are opted for as no adverse cellular response have been reported (Ref 25,26). WE43B is a new class of Mg alloy with Y and Nd as the main alloying elements and is among the few Mg alloys with practical application in biomedical implant technology (Ref 27). It is therefore of great importance to understand the corrosion behavior of WE43B in the physiological system.

The dynamic electrochemical impedance spectroscopy (DEIS) is relatively a new technique developed for the measurement of impedance through the application of Short-Time Fourier Transform (STFT) coupled with multi-sinusoid perturbation signal. This technique is designed to be able to track electrochemical changes on surfaces in non-stationary systems with time, potential, current, and temperature (Ref 28), a feature that is lacking in the classical EIS. As it is known (Ref 29)(Ref 30), the classical EIS technique demands that three cardinal conditions of causality (the measured impedance response is due only to the AC perturbation applied), linearity (a small AC perturbations, usually 1 to 10 mV is applied), and stability (the

system returns to its original state after the perturbation is removed and does not change with time) be met for the EIS data to be valid. In practice, these conditions especially the steady state conditions can be difficult to achieve. The system can change through adsorption of inhibitors or impurities, the growth of an oxide layer, the build-up or degradation of corrosion products, change in the system temperature, etc. The DEIS technique is thus designed to overcome these challenges. This technique had been used in corrosion inhibition studies and results corroborated with results from other techniques including the hydrogen evolution technique (Ref 31).

The aim of this work is to scrutinize the corrosion characteristics of WE43B alloy in a simulated body fluid (SBF) at a typical body temperature. The DEIS is used in combination with other classical techniques namely, linear polarization, EIS, potentiodynamic polarization, and the hydrogen evolution to track the corrosion pattern of the alloy in SBF for 24 h at 37 °C.

2. Materials and Experimental details

The WE43B alloy was purchased from Goodfellow Cambridge Limited, Ermine Business Park Huntingdon, United Kingdom (Ref 27). The chemical composition of WE43B in wt.% is as follow: Y (4), Nd (3), Zr (0.4), rare-earth mischmetal (1), and the balance is Mg (Ref 32,33). The optimal properties of WE43B alloy are developed when it is fully heat treated. The process involves solution heat treatment for 8 h at 525°C follows by air cooling and subsequent aging for 16 h at 250°C before the final air cooling (Ref 32). The WE43B sample was soldered to a copper wire and mounted using an epoxy resin to get the working electrode for the electrochemical experiments with an exposed surface area of 10 cm^2. The mounted samples were mechanically abraded using 800-2000 grade of abrasive paper and cleaned using the procedure previously described (Ref 34,35).

The chemical composition of the simulated body fluid (SBF) solution is as listed in Table 1. SBF was prepared following the procedure recommended by Kokubo and Takadama (Ref 36). Briefly, a 1000 mL capacity plastic beaker was filled with 700 mL of deionized water and covered with watch glass. It was set in a thermostatic water bath, stirred, and the temperature maintained at 37 °C. The reagents at Nos. 1 – 8 in Table 1 were dissolved one after the other following the order listed in the table. Thereafter, the reagent at No. 9 was added to the colorless and transparent solution followed by HCl in drops to adjust the pH to the required 7.4.

Table 1: Chemical Composition of the SBF (Ref 37).

S/N	Chemical	Amount (grams in 1000 mL)

1	NaCl	8.035
2	$NaHCO_3$	0.355
3	KCl	0.225
4	$K_2HPO_4.3H_2O$	0.231
5	$MgCl_2.H_2O$	0.311
6	1 M HCl	40 mL
7	$CaCl_2$	0.292
8	Na_2SO_4	0.072
9	$((CH_2OH)_3CNH_2)$	6.118
10	1 M HCl	Appropriate amount for adjusting the pH 7.4

The set-up for the DEIS measurements can be found in our previous publications (Ref 38,39). The current perturbation was generated using a National Instruments Ltd. PCI-4461 digital–analog card, which also performed the task of recording current and voltage signals (Ref 38–40). The frequency of the excitation signal was in the range of 4.5 kHz – 300 mHz. The electrochemical characteristics of the WE43B sample was recorded for 24 h at 37 °C. The evolution of hydrogen gas was concurrently measured during the DEIS experiments. The experimental set up for the volumetric experiments is shown in Figure 1. After the DEIS and volumetric experiments, the EIS and potentiodynamic (PDP) measurements were undertaken using a Gamry 600 system. In all the experiments, the 200 mL of the SBF was used and the initial and final pH were 7.4 and 8.58, respectively. The abraded WE43B sample with surface area of 10 cm^2 was the working electrode, Ag/AgCl was the reference electrode, and a platinum plate acted as the counter electrode. The frequency range for the classical EIS was 5.2 kHz – 30 mHz while the potential range for the PDP experiments was −250 to +250 mV versus open circuit potential utilizing a scan rate of 1 mV/s. It should be mentioned that the PDP measurements were the last sets of experiments and were done after 24 h. The electrochemical parameters were obtained using the Echem Analyst software. For the linear polarization (LPR) experiments, a special experimental procedure was developed with Nova 2.1.5 software such that LPR data were automatically recorded at 30-minute interval for 24 h at a potential range of ± 10 mV and scan rate of 0.125 mV/s. At the end of the LPR experiments, the samples were submitted for surface morphology examination which was performed using a scanning electron microscope (SEM) J. Quanta FEG 250 model (FEI, Holland) and a Park Systems XE-100E model atomic force microscope. The SEM is coupled to energy-dispersive X-ray spectroscopy (EDX) for composition determination. Surface roughness analysis was performed using atomic force microscopy (AFM), the Park System X-100E AFM model.

3. Results and discussion

The WE43B, as mentioned in the introduction is one of the few magnesium alloys with a practical application as a biomedical implant material (Ref 27), hence the study of the corrosion characteristics of this alloy is essential. The impedance spectra obtained for the WE43B sample in a simulated body fluid (SBF) for 24 h at 37 °C using the DEIS technique are shown in Fig. 2. Similar to previous reports (Ref 41–43), the Nyquist spectra exhibit two capacitive loops at high and medium frequencies. The semi-circular curve at the high-frequency region is due to the charge-transfer resistance and the double-electric layer capacitance at the interface (Ref 41–43) while the second capacitive loop is caused by the mass transportation through the corrosion product layer (Ref 41). A close inspection of Fig. 2 reveals that the diameter of the two capacitive loops increase with increase in immersion time reflecting the increase in the charge transfer resistance (R_{ct}) as well as polarization resistance (R_p) with time. This is also clearly seen in the R_{ct} versus time and the R_p versus time graphs given in Fig. 3.

Generally, a $Mg(OH)_2$ layer is formed during the initial corrosion of Mg and its alloy in a SBF solution (Ref 41–43). The $Mg(OH)_2$ layer is porous and dissolves to form $MgCl_2$ in high chloride content solution (Ref 41). The lower R_{ct} and R_p values observed at the early stages of immersing WE43B sample in the SBF solution (Fig. 3) is related to the less protective ability of the $Mg(OH)_2$ layer. The porous nature of the layer makes it easier for corrosive ions to penetrate the magnesium substrate. The SEM image shown in Fig. 4(c) support this assertion. Cracks of various dimension are seen on corrosion product layer on WE43B surface. Corrosive species could easily penetrate through these cracks and get to the substrate surface especially at the early stage of corrosion that the corrosion layer is still very porous. Nevertheless, Figs. 2 and 3 disclose that the corrosion resistance of the alloy constantly improved with time. The EDX results in Fig. 4(d & e) and in Table 1 provide insight into the nature of the corrosion products at prolonged immersion duration. The corrosion product is enriched with Mg, Y, Nd, C, O, P, Ca, and Zn suggesting a mixture of oxides such as MgO, Nd_2O_3, Y_2O_3, and apatite, which according to Rettig et al. (Ref 44), has the composition $(Mg, Ca)_x(PO_4)_y(CO_3)_z(OH)_i$. It means that the alloying elements diffused from the alloy matrix to the surface and formed a protective layer. As revealed by Fig. 4(a) and Table 1, after 24 h of immersion, higher percentage of Nd and Y were detected in both Spot 1 & 2 (Fig. 4(d & e)) relative to the uncorroded surface (Fig. 4(b)). Jin *et al*. (Ref 41) in their investigation on the effect of Nd self-ion implantation on the corrosion resistance of WE43 Mg alloy in SBF found that, Nd

implantation significantly enhanced the corrosion resistance of the WE43 Mg alloy. The corrosion product layer was found to consist of Nd_2O_3 as the outer and MgO as the inner layers. The Nd_2O_3 outer layer was found to be stable and mainly responsible for the anticorrosion property while the inner MgO layer reinforced the protection of the WE43 Mg alloy. Other authors (Ref 45–47) had equally reported the positive influence of Nd on the corrosion resistance property of Mg alloys especially the Al-containing Mg alloys where the α grains significantly refined and large amounts of Al–Nd phases concentrated at the grain boundaries and separate the α grains such that the propagation of corrosion becomes more difficult (Ref 43).

Yttrium, depending on the alloying concentration can accelerate corrosion of Mg alloys or enhance the corrosion resistance property (Ref 42). Corrosion resistance is enhanced when the added Y is less than 0.3 wt.% for the AZ91 alloys (Ref 48), 2 wt.% for the Mg–3Al alloys (Ref 49), and 2.5 wt.% for the Mg-Y alloys (Ref 50). Baek *et al*. (Ref 51) claimed that the corrosion resistance of Mg-Al-Ca-Y alloy containing 0.25 wt.% Y was greatly improved as a result of the change in Al-containing intermetallic particles due to the formation of less noble Al_8Mn_4Y or Al_2Y phases associated with a reduction in the rate of hydrogen evolution during corrosion process. Li *et al*. (Ref 52) reported an improvement on the corrosion resistance of Mg-6%Al-3%Zn through alloying with Y which gave rise to the increasing content of Al_2O_3 in oxide layer. In this work, judging from the constant increase in the corrosion resistance property of the WE43B with time (Figs. 2 & 3), it could be concluded that the corrosion product layer formed by the Nd and Y alloying elements benefitted the corrosion resistance of the alloy.

Table 2. EDX analysis for WE43B alloy before and after LPR corrosion measurement test in simulated body fluid at 37 °C.

WE43B	Section	Atomic %								
		Mg	Y	Nd	C	O	P	Ca	Zn	Total
Before corrosion tests	Full area	98.15	1.21	0.64	-	-	-	-	-	100
After 24 h LPR measurements	Spot 1	4.39	3.65	2.39	10.49	15.64	26.03	36.17	1.24	100
	Spot 2	85.27	7.93	6.80	-	-	-	-	-	100

The measurement of the rate of hydrogen gas (H_2) evolution is one of the simplest and accurate methods for studying the corrosion rate of magnesium in aqueous media. Based on the elements detected on the corrosion products (Fig. 4 and Table 2), the anodic reactions can be written as:

$$Mg \rightarrow Mg^{2+} + 2e^{-} \quad (1)$$

$$Nd \rightarrow Nd^{3+} + 3e^{-} \quad (2)$$

$$Y \rightarrow Y^{3+} + 3e^{-} \quad (3)$$

The corresponding cathodic reaction is as given in Eq. 4 (Ref 42):

$$2H_2O + 2e^{-} \rightarrow H_2 + 2OH^{-} \quad (4)$$

The total reaction is:

$$Mg + 2H_2O \rightarrow Mg(OH)_2 + H_2 \quad (5)$$

$$2Nd + 6H_2O \rightarrow 2Nd(OH)_3 + 3H_2 \quad (6)$$

$$2Y + 6H_2O \rightarrow 2Y(OH)_3 + 3H_2 \quad (7)$$

The conversion of $Nd(OH)_3$ and $Y(OH)_3$ to Nd_2O_3 and Y_2O_3, respectively occurs through a solid phase transformation reaction (Eqs. 8 & 9) (Ref 42):

$$2Nd(OH)_3 \rightarrow Nd_2O_3 + 3H_2O \quad (8)$$

$$2Y(OH)_3 \rightarrow Y_2O_3 + 3H_2O \quad (9)$$

Equation 5 implies that, for each Mg^{2+} ion produced in the anodic region, one molecule of H_2 is evolved at the cathodic region. Hence, the rate of hydrogen evolution can be equated to the corrosion rate of Mg. Corrosion rate of Mg obtained from other techniques such as the weight loss and electrochemical techniques has been reported to compare considerably with that from the hydrogen evolution technique (Ref 53)(Ref 54). Figure 5(a) shows the evolution of hydrogen gas with time as monitored during the DEIS experiments on the corrosion of WE43B implant rod in simulated body fluid at 37 °C. From the hydrogen evolution results, the corrosion current density (i_{corr}) and corrosion rate (CR) were calculated using Eqs. 10 and 11, respectively (Ref 55,56).

$$i_{corr}\ (\mathrm{A\ cm^{-2}}) = \frac{2pVF}{tSRT} \quad (10)$$

$$CR\ (\mathrm{mm\ y^{-1}}) = \frac{j_{corr} K E_W}{dS} \quad (11)$$

where p is pressure in Pascal (101325 P), V is the volume of hydrogen gas (cm^3) evolved in time t (h), F is Faraday's constant (96485 C/mol), S is the surface area of the sample in cm^2, R is the molar gas constant (8.314 m^2 kg s^{-2} K^{-1} mol^{-1}), T is temperature in kelvin (310 K), K is equal to 3272 and is the conversion factor, E_W is the equivalent weight (12.74 amu), and d the density in g/cm^3. The plots of the variation of corrosion rate, corrosion current density, and the

B value against time for the corrosion of WE43B alloy in simulated body fluid at 37 °C are given in Fig. 5(b-d). There was a rapid evolution of hydrogen gas in the first 9 h of immersion of the sample (Fig. 5(a)). Beyond this time, the volume of gas evolved significantly diminished. Figs. 5(b) and (c) reveal that the corrosion rate and the corrosion current density steadily decreased with immersion time. It is required that an ideal biodegradable metal implant, beside biocompatibility, corrodes with appropriate corrosion rate that makes it remain stable for several months before it is completely bio-absorbed (Ref 57). According to (Ref 58,59), the permissible corrosion rate for medical implants is 0.4 mm y^{-1}. At 24 h, the value of 1.326 mm y^{-1} is obtained for WE43B alloy from hydrogen evolution technique. Based on Stern Geary equation (Eq.12) and making use of the i_{corr} from the volumetry experiments and charge transfer resistance (R_{ct}) from the DEIS, the *B* factor in Eq.12 was calculated. The variation of *B* against time for the corrosion of WE43B alloy in simulated body fluid at 37 °C is shown in Fig. 5(d). The *B* factor is decreasing with time implying that the corrosion process is changing with time (Ref 60) and thus confirmed the DEIS results (Fig. 2).

$$i_{corr} = \frac{b_a b_c}{2.303(b_a + b_c)} \frac{1}{R_{ct}} = \frac{B}{R_{ct}} \qquad (12)$$

Figure 6(a) shows the impedance characteristic of the WE43B implant rod in simulated body fluid at 37 °C after 24 h of immersion as obtained from the classical electrochemical impedance spectroscopy technique. The impedance spectrum is characterized by two capacitive loops at the high and the medium frequencies. Obviously, one of the capacitive loops would correspond to the charge transfer processes and the other to mass transport processes related to the migration of ions through adsorbed corrosion product layer (Ref 61). Because of this observation, two equivalent circuit models were used in fitting the impedance data. The first was the $R(Q_1(R_1(Q_2R_2)))$ model which defines the layer resistance and the second was the $R(Q_1R_1(Q_2R_2))$ model which explains the adsorption resistance. From the layer resistance model, R_1 = 928 Ω cm^2 and R_2 = 470 Ω cm^2. Similarly, the adsorption model gives R_1 = 1398 Ω cm^2 and R_2 = 2762 Ω cm^2. The Stern Geary relationship given in Eq. 12 can be used to check which of the *R*s denotes the R_{ct} by calculating the corrosion current density (i_{corr}) and comparing with the i_{corr} value obtained from the potentiodynamic polarization method. By using the R_1 and R_2 values gotten with the layer resistance model, the calculated i_{corr} value is 97.51 μA/cm^2 and 192.58 μA/cm^2, respectively. Also, 64.76 μA/cm^2 and 32.78 μA/cm^2, respectively are obtained as i_{corr} value by using the R_1 and R_2 values obtained with the

adsorption resistance model. Meanwhile, the i_{corr} value obtained for WE43B alloy in simulated body fluid at 37 °C from the potentiodynamic polarization and linear polarization techniques is 64 μA/cm^2 and 65 μA/cm^2, respectively which is comparable with the value obtained using R_1 value of the adsorption resistance model. Therefore, the proper model is the adsorption resistance model [$R(Q_1R_1(Q_2R_2))$] and the first capacitive loop represents the charge transfer controlled corrosion process (Ref 62). The charge transfer resistance value (1398 Ω cm^2) obtained from the electrochemical impedance spectroscopy technique and the polarization resistance value (1433 Ω cm^2) obtained from the linear polarization technique at 24 h of measurements are comparable.

Figure 6(b) shows the comparative graphs of the impedance spectra obtained from the classical EIS and the DEIS after 24 h of exposition. As could be seen, the spectra are comparable and exhibit two capacitive loops. The incomplete second semi-circle seen in the DEIS spectrum is because the low frequency perturbation used in the DEIS was 300 mHz whereas 30 mHz was used in the classical-EIS.

The potentiodynamic polarization plot obtained for the WE43B sample after 24 h of exposure at 37 °C is shown in Fig. 7. The parameters namely, the i_{corr}, anodic and cathodic slope (β_a and β_c), and the corrosion rate (CR) were obtained by extrapolating the linear portion of the plot. The i_{corr} value obtained is 64.0 μA/cm^2, the β_a and β_c values are 0.481 V/dec and 0.368 V/dec, respectively while the CR is 1.326 mm y^{-1}. The plot reveals that the alloy undergoes an active anodic oxidation and cathodic hydrogen ions reduction corrosion processes. However, the i_{corr} and CR values, relative to previous reports indicate that the WE43B alloy is less susceptible to electrochemical corrosion in SBF. Zhou *et al*. (Ref 1) reported the i_{corr} and CR values of 74 μA/cm^2 and 1.62 mm y^{-1}, respectively in SBF at 37 °C after 24 h of immersion for ageing treated AZ91D alloy. Rai *et al*. (Ref 7) reported CR value of 191.785 mm y^{-1} for magnesium based 1393 bioactive glass in SBF after 24 h of exposure. There is a good correlation between the corrosion rates determined from the i_{corr} value from the hydrogen evolution, linear polarization, and the potentiodynamic polarization techniques (Fig. 7(b)). Generally, the hydrogen evolution method is most suitable for corrosion reactions in which the cathodic reactions involved the evolution of H_2 and the corrosion rate from this technique relates to corrosion averaged over a considerable length of time and includes corrosion of some considerable time after corrosion onset, when the corrosion is well established (Ref 1). The LPR is a non-destructive technique, a fast way of detecting corrosion rate, and the corrosion rate measured is related to the onset of corrosion (Ref 63). However,

the fundamental disadvantage of LPR is that in order to convert polarization resistance to corrosion rate, the Tafel parameters must be known (Ref 63). The PDP in the other hands includes a simple and clear method for determining Tafel parameters β_a and β_c unlike the LPR and can provide precise information about the corroding metal's active, passive, and trans–passive characteristics (Ref 63). However, it is a destructive technique because of the high current density required to completely polarize a metal surface (Ref 63). In this study, as expected, the *CR* value from the three techniques is in the order: Hydrogen evolution (1.326 mm y^{-1}) < LPR (1.337 mm y^{-1}) < PDP (1.338 mm y^{-1}). However, the corrosion rate obtained for WE43B in this study is higher than 0.4 mm y^{-1} claimed as the tolerable maximum corrosion rate for biomaterial intended for implant applications (Ref 58,59). This makes the suitability of WE43B for long-term implant application worrisome. Nevertheless, WE43B has the advantage of not containing the characteristic impurities namely Fe, Cu, Ni, and Be (Ref 64). As it is known (Ref 64), Be concentration is limited to 4 ppm, Cu is limited to 100– 300 ppm, Fe to 35–50 ppm, and Ni is not expected to exceed 20– 50 ppm. The rare earth elements contained in WE43B fall under 'other chemical elements' referred to as normal alloying elements in which their limits are given together with the nominal contents of alloying elements (Ref 64). It should however be mentioned that rare earth elements exhibit anticancerogenic properties (Ref 64), hence must be kept minimal.

The roughness characteristics of the alloy before and after immersion in SBF for 24 h at 37 ^{o}C are presented in Fig. 8. The AFM technique has found application in corrosion studies and in most cases, small values of the surface roughness parameters are interpreted to infer minimal corrosion (Ref 1). It is, however pertinent to mention that, surface roughness parameters used in isolation to quantify surface susceptibility could be misleading as corrosion products could be evenly distributed to give low values of surface parameters. In this work, the roughness parameters are defined thus: R_{ku} is the kurtosis, R_{sk} is the skewness, R_z is the maximum height, R_a is the arithmetic mean height, R_q is the root mean square height, and R_{pv} is the maximum pit height (Ref 65)(Ref 66). As seen in Fig. 8, the surface roughness increased upon immersion of the sample in SBF due to corrosion. A comparison of the values of the roughness parameters for Fig. 8(a) to those of Fig. 8(b) reveals that the difference is not too significant and may indicate that the deterioration of the alloy in the SBF was not very severe. For instance, the difference for the R_a, R_{ku}, and R_q parameters is 9.5488 nm, 1.2845 nm, and 15.453 nm, respectively. This agrees with other results that the WE43B sample is less susceptible to corrosion in SBF relative to other Mg alloys (Ref 1).

4. Conclusions

1) The alloy corroded in SBF exhibiting a typical impedance characteristic of Mg consisting of two capacitive loops at high and medium frequencies.
2) The polarization resistance (R_p) WE43B steadily increased while the corrosion rate (*CR*) decreased with immersion time. At 24 h of immersion, *CR* of the alloy is in the range of 1.326 – 1.338 mm y^{-1}.
3) There is a good correlation between the corrosion rates obtained from the hydrogen evolution, linear polarization, and the potentiodynamic techniques. The surface analysis (SEM, EDX, AFM) results conform with the results obtained from the applied methods.
4) The results indicate that corrosion rate of WE43B alloy is higher than the 0.4 mm y^{-1} permissible corrosion rate for medical implants (Ref 58,59). Because the corrosion rate is still decreasing at the maximum duration (24 h) considered, a longer-term corrosion studies is recommended.

Acknowledgements

This research work was partly supported by Scientific and Technological Research Council of Turkey TUBITAK-BIDEB 2224-A and TUBITAK 2219- International Postdoctoral Research Fellowship (Program Project Number: 1059B191900111).

References

1. W. Zhou, T. Shen, and N.N. Aung, Effect of Heat Treatment on Corrosion Behaviour of Magnesium Alloy AZ91D in Simulated Body Fluid, *Corros. Sci.*, Elsevier Ltd, 2010, **52**(3), p 1035–1041, doi:10.1016/j.corsci.2009.11.030.

2. C. Zhang, X. Huang, M. Zhang, L. Gao, and R. Wu, Electrochemical Characterization of the Corrosion of a Mg-Li Alloy, *Mater. Lett.*, 2008, **62**(14), p 2177–2180.

3. A. Doepke, D. Xue, Y. Yun, W.J. Vanooij, H. Brian Halsall, and W.R. Heineman, Corrosion of Organosilane Coated Mg4Y Alloy in Sodium Chloride Solution Evaluated by Impedance Spectroscopy and PH Changes, *Electrochim. Acta*, Elsevier Ltd, 2012, **70**, p 165–170, doi:10.1016/j.electacta.2012.03.040.

4. S.S. Jamali, S.E. Moulton, D.E. Tallman, M. Forsyth, J. Weber, and G.G. Wallace, Evaluating the Corrosion Behaviour of Magnesium Alloy in Simulated Biological Fluid by Using SECM to Detect Hydrogen Evolution, *Electrochim. Acta*, Elsevier Ltd,

2015, **152**, p 294–301, doi:10.1016/j.electacta.2014.11.012.

5. Y. Liu, M. Curioni, and Z. Liu, Correlation between Electrochemical Impedance Measurements and Corrosion Rates of Mg-1Ca Alloy in Simulated Body Fluid, *Electrochim. Acta*, Elsevier Ltd, 2018, **264**, p 101–108, doi:10.1016/j.electacta.2018.01.121.

6. T. Zhu, Y. Yu, J. Yang, Y. Shen, L. He, and Y. Xiong, Dynamic Corrosion Behavior of AZ80 Magnesium Alloy with Different Orientations in Simulated Body Fluid, *Mater. Chem. Phys.*, 2021, **259**(November 2020).

7. P. Rai, A. Rai, V. Kumar, R.K. Chaturvedi, and V.K. Singh, Corrosion Study of Biodegradable Magnesium Based 1393 Bioactive Glass in Simulated Body Fluid, *Ceram. Int.*, Elsevier Ltd and Techna Group S.r.l., 2019, **45**(14), p 16893–16903, doi:10.1016/j.ceramint.2019.05.234.

8. S. Sharma and A. Kumar, Recent Advances in Metallic Corrosion Inhibition: A Review, *J. Mol. Liq.*, Elsevier, 2021, **322**, p 114862.

9. A. Balamurugan, S. Rajeswari, G. Balossier, A.H.S. Rebelo, and J.M.F. Ferreira, Corrosion Aspects of Metallic Implants - An Overview, *Mater. Corros.*, John Wiley & Sons, Ltd, 2008, **59**(11), p 855–869, doi:10.1002/maco.200804173.

10. M. Esmaily, J.E. Svensson, S. Fajardo, N. Birbilis, G.S. Frankel, S. Virtanen, R. Arrabal, S. Thomas, and L.G. Johansson, "Fundamentals and Advances in Magnesium Alloy Corrosion," *Progress in Materials Science*, 2017, p 92–193.

11. Y. Sasikumar, M.M. Solomon, L.O. Olasunkanmi, and E.E. Ebenso, Effect of Surface Treatment on the Bioactivity and Electrochemical Behavior of Magnesium Alloys in Simulated Body Fluid, *Mater. Corros.*, 2017, **68**(7), p 776–790.

12. S.V.S. Prasad, S.B. Prasad, K. Verma, R.K. Mishra, V. Kumar, and S. Singh, The Role and Significance of Magnesium in Modern Day Research-A Review, *J. Magnes. Alloy.*, Elsevier, 2022, **10**(1), p 1–61.

13. M. Gupta and N.M.L. Sharon, Magnesium, Magnesium Alloys, and Magnesium Composites, *Magnesium, Magnes. Alloy. Magnes. Compos.*, John Wiley and Sons, 2010, **620**(978), p 87–109, doi:10.1002/9780470905098.

14. V. Kaesel, P.-T. Tai, F.-W. Bach, H. Haferkamp, F. Witte, and H. Windhagen,

Approach to Control the Corrosion of Magnesium by Alloying, *Magnesium*, John Wiley & Sons, Ltd, 2005, p 534–539, doi:10.1002/3527603565.CH84.

15. H.R. Bakhsheshi-Rad, M.R. Abdul-Kadir, M.H. Idris, and S. Farahany, Relationship between the Corrosion Behavior and the Thermal Characteristics and Microstructure of Mg-0.5Ca-XZn Alloys, *Corros. Sci.*, 2012, **64**, p 184–197, doi:10.1016/j.corsci.2012.07.015.

16. Q. Zhang, Q. Li, and X. Chen, Effect of Heat Treatment on Corrosion Behavior of Mg–5Gd–3Y–0.5Zr Alloy, *RSC Adv.*, The Royal Society of Chemistry, 2020, **10**(71), p 43371–43382, doi:10.1039/D0RA08933H.

17. C. Gül, S. Albayrak, H. Çinici, and A. Aytaç, Improvement in Corrosion Resistance of Tantalum Oxide and Tantalum Oxide with Diethanolamine Sol–Gel Coated Magnesium Alloys, *Prot. Met. Phys. Chem. Surfaces*, Pleiades Publishing, 2022, **58**(3), p 603–614, doi:10.1134/S2070205122030108/FIGURES/11.

18. C. Gül, S. Albayrak, and H. Çinici, Characterization of Tantalum Oxide Sol–Gel-Coated AZ91 Mg Alloys, *Trans. Indian Inst. Met.*, Springer, 2020, **73**(5), p 1249–1256, doi:10.1007/S12666-020-01976-Y/FIGURES/10.

19. H.R. Bakhsheshi-Rad, E. Hamzah, H.Y. Tok, M. Kasiri-Asgarani, S. Jabbarzare, and M. Medraj, Microstructure, In Vitro Corrosion Behavior and Cytotoxicity of Biodegradable Mg-Ca-Zn and Mg-Ca-Zn-Bi Alloys, *J. Mater. Eng. Perform.*, Springer New York LLC, 2017, **26**(2), p 653–666, doi:10.1007/S11665-016-2499-0/FIGURES/14.

20. M. Razzaghi, M. Kasiri-Asgarani, H.R. Bakhsheshi-Rad, and H. Ghayour, In Vitro Degradation, Antibacterial Activity and Cytotoxicity of Mg-3Zn-XAg Nanocomposites Synthesized by Mechanical Alloying for Implant Applications, *J. Mater. Eng. Perform.*, Springer New York LLC, 2019, **28**(3), p 1441–1455, doi:10.1007/S11665-019-03923-5/FIGURES/13.

21. J.L. Domingo, Reproductive and Developmental Toxicity of Aluminum: A Review, *Neurotoxicol. Teratol.*, Pergamon, 1995, **17**(4), p 515–521.

22. M. Peron, J. Torgersen, and F. Berto, Mg and Its Alloys for Biomedical Applications: Exploring Corrosion and Its Interplay with Mechanical Failure, *Metals (Basel).*, 2017,

7(7), p 1–41.

23. T.P. Flaten, Aluminium as a Risk Factor in Alzheimer's Disease, with Emphasis on Drinking Water, *Brain Res. Bull.*, Elsevier, 2001, **55**(2), p 187–196.

24. S.S. Abd El-Rahman, Neuropathology of Aluminum Toxicity in Rats (Glutamate and GABA Impairment), *Pharmacol. Res.*, Academic Press, 2003, **47**(3), p 189–194.

25. C. Wang, J. Park, C. Ouyang, J.A. Longmate, M. Tajon, J. Chao, D. Lim, J. Sandhu, H.H. Yin, R. Pillai, M.C. Gozo, C. Avalos, C.A. Egelston, P.P. Lee, and M. Fakih, A Pilot Feasibility Study of Yttrium-90 Liver Radioembolization Followed by Durvalumab and Tremelimumab in Patients with Microsatellite Stable Colorectal Cancer Liver Metastases, *Oncologist*, Oxford University Press, 2020, **25**(5), p 382, doi:10.1634/THEONCOLOGIST.2019-0924.

26. S.T. Rajan, M. Das, and A. Arockiarajan, Biocompatibility and Corrosion Evaluation of Niobium Oxide Coated AZ31B Alloy for Biodegradable Implants, *Colloids Surfaces B Biointerfaces*, Elsevier, 2022, **212**, p 112342.

27. Goodfellow, "List of Products for Magnesium Alloy WE43B - Mg93/Y4/Nd3 -," *GoodFellow ,Seoul Finance Center, 4F, 136 Sejong-daero, Jung-gu, Seoul, 04520*, n.d., https://www.goodfellow.co.kr/en/material/magnesium-alloy-we43b-MG11.htm. Accessed 19 May 2022.

28. K. Darowicki, Theoretical Description of the Measuring Method of Instantaneous Impedance Spectra, *J. Electroanal. Chem.*, Elsevier Sequoia SA, 2000, **486**(2), p 101–105.

29. S. Cruz-Manzo, R. Chen, P. Greenwood, and □ S Cruz-, Evaluate the Validity of Electrochemical Impedance Measurements of Polymer Electrolyte Fuel Cells Using a Computational Algorithm Based on Fast Fourier Transform, *Insights Anal. Electrochem.*, Prime Scholars, 2015, **1**(1), p 1–12, doi:10.21767/2470-9867.100003.

30. Gamry.com, "Basics of EIS: Electrochemical Research-Impedance," 2022, https://www.gamry.com/application-notes/EIS/basics-of-electrochemical-impedance-spectroscopy/. Accessed 8 May 2022.

31. P. Slepski, H. Gerengi, A. Jazdzewska, J. Orlikowski, and K. Darowicki, Simultaneous Impedance and Volumetric Studies and Additionally Potentiodynamic Polarization

Measurements of Molasses as a Carbon Steel Corrosion Inhibitor in 1M Hydrochloric Acid Solution, *Constr. Build. Mater.*, Elsevier, 2014, **52**, p 482–487.

32. Luxfer Mel Technologies, "Elektron® WE43B | High Strength Alloy | Luxfer MEL Technologies," n.d., https://www.luxfermeltechnologies.com/products/elektron-we43b/. Accessed 3 June 2023.

33. S. Agnew, W. Whittington, A. Oppedal, H. El Kadiri, M. Shaeffer, K.T. Ramesh, J. Bhattacharyya, R. Delorme, and B. Davis, Dynamic Behavior of a Rare-Earth-Containing Mg Alloy, WE43B-T5, Plate with Comparison to Conventional Alloy, AM30-F, *JOM*, Springer, 2014, **66**(2), p 277–290, doi:10.1007/S11837-013-0830-X/TABLES/3.

34. ASTM G102, Standard Practice for from Electrochemical Measurements, *ASTM*, 2015, **89**(Reapproved 2015), p 1–7.

35. G.-90 ASTM, "Standard Practice for Preparing, Cleaning, and Evaluating Corrosion Test Specimens," n.d., https://www.astm.org/DATABASE.CART/HISTORICAL/G1-90R99E1.htm. Accessed 8 November 2019.

36. T. Kokubo and H. Takadama, How Useful Is SBF in Predicting in Vivo Bone Bioactivity?, *Biomaterials*, Elsevier BV, 2006, **27**(15), p 2907–2915.

37. H. Gerengi, M. Cabrini, M.M. Solomon, and E. Kaya, Understanding the Corrosion Behavior of the AZ91D Alloy in Simulated Body Fluid through the Use of Dynamic EIS, *ACS Omega*, American Chemical Society (ACS), 2022, **7**(14), p 11929–11938, doi:10.1021/ACSOMEGA.2C00066/ASSET/IMAGES/MEDIUM/AO2C00066_M006.GIF.

38. P. Slepski, M. Szocinski, G. Lentka, and K. Darowicki, Novel Fast Non-Linear Electrochemical Impedance Method for Corrosion Investigations, *Meas. J. Int. Meas. Confed.*, Elsevier B.V., 2021, **173**, p 108667.

39. P. Slepski, H. Gerengi, G. Gece, E. Kaya, M. Rizvi, and M. Szociński, Electrochemical Evaluation of Sustainable Corrosion Inhibitors via Dynamic Electrochemical Impedance Spectroscopy, *ACS Symp. Ser.*, American Chemical Society, 2021, **1403**, p 61–85.

40. H. Gerengi, M. Mielniczek, G. Gece, and M.M. Solomon, Experimental and Quantum

Chemical Evaluation of 8-Hydroxyquinoline as a Corrosion Inhibitor for Copper in 0.1 M HCl, *Ind. Eng. Chem. Res.*, 2016, **55**(36).

41. W. Jin, G. Wu, H. Feng, W. Wang, X. Zhang, and P.K. Chu, Improvement of Corrosion Resistance and Biocompatibility of Rare-Earth WE43 Magnesium Alloy by Neodymium Self-Ion Implantation, *Corros. Sci.*, Pergamon, 2015, **94**, p 142–155.

42. X. Liu, D. Shan, Y. Song, and E. hou Han, Influence of Yttrium Element on the Corrosion Behaviors of Mg–Y Binary Magnesium Alloy, *J. Magnes. Alloy.*, National Engg. Reaserch Center for Magnesium Alloys, 2017, **5**(1), p 26–34.

43. J. Zhang, J. Wang, X. Qiu, D. Zhang, Z. Tian, X. Niu, D. Tang, and J. Meng, Effect of Nd on the Microstructure, Mechanical Properties and Corrosion Behavior of Die-Cast Mg-4Al-Based Alloy, *J. Alloys Compd.*, 2008, **464**(1–2), p 556–564.

44. R. Rettig and S. Virtanen, Composition of Corrosion Layers on a Magnesium Rare-Earth Alloy in Simulated Body Fluids, *J. Biomed. Mater. Res. Part A*, John Wiley & Sons, Ltd, 2009, **88A**(2), p 359–369, doi:10.1002/JBM.A.31887.

45. M.T. Majd, T. Shahrabi, and B. Ramezanzadeh, The Role of Neodymium Based Thin Film on the Epoxy/Steel Interfacial Adhesion and Corrosion Protection Promotion, *Appl. Surf. Sci.*, North-Holland, 2019, **464**, p 516–533.

46. Y.L. Song, Y.H. Liu, S.R. Yu, X.Y. Zhu, and Q. Wang, Plasma Electrolytic Oxidation Coating on AZ91 Magnesium Alloy Modified by Neodymium and Its Corrosion Resistance, *Appl. Surf. Sci.*, North-Holland, 2008, **254**(10), p 3014–3020.

47. J. Zhang, J. Wang, X. Qiu, D. Zhang, Z. Tian, X. Niu, D. Tang, and J. Meng, Effect of Nd on the Microstructure, Mechanical Properties and Corrosion Behavior of Die-Cast Mg–4Al-Based Alloy, *J. Alloys Compd.*, Elsevier, 2008, **464**(1–2), p 556–564.

48. T.J. Luo and Y.S. Yang, Corrosion Properties and Corrosion Evolution of As-Cast AZ91 Alloy with Rare Earth Yttrium, *Mater. Des.*, Elsevier, 2011, **32**(10), p 5043–5048.

49. M. Nouri, X. Sun, and D.Y. Li, Beneficial Effects of Yttrium on the Performance of Mg–3%Al Alloy during Wear, Corrosion and Corrosive Wear, *Tribol. Int.*, Elsevier, 2013, **67**, p 154–163.

50. X. Zhang, K. Zhang, X. Deng, L. Hongwei, L. Yongjun, M. Minglong, L. Ning, and Y.

Wang, Corrosion Behavior of Mg–Y Alloy in NaCl Aqueous Solution, *Prog. Nat. Sci. Mater. Int.*, Elsevier, 2012, **22**(2), p 169–174.

51. S.M. Baek, J.S. Kang, H.J. Shin, C.D. Yim, B.S. You, H.Y. Ha, and S.S. Park, Role of Alloyed Y in Improving the Corrosion Resistance of Extruded Mg–Al–Ca-Based Alloy, *Corros. Sci.*, Pergamon, 2017, **118**, p 227–232.

52. J. Li, Z. Chen, J. Jing, and J. Hou, Effect of Yttrium Modification on the Corrosion Behavior of AZ63 Magnesium Alloy in Sodium Chloride Solution, *J. Magnes. Alloy.*, Elsevier, 2021, **9**(2), p 613–626.

53. G. Song, A. Atrens, and D. StJohn, An Hydrogen Evolution Method for the Estimation of the Corrosion Rate of Magnesium Alloys, *Essential Readings in Magnesium Technology*, Springer, Cham, 2016, p 565–572, doi:10.1007/978-3-319-48099-2_90.

54. S.A.S.A. Umoren, M.M.M. Solomon, A. Madhankumar, and I.B.I.B. Obot, Exploration of Natural Polymers for Use as Green Corrosion Inhibitors for AZ31 Magnesium Alloy in Saline Environment, *Carbohydr. Polym.*, Elsevier Ltd, 2020, **230**, p 115466.

55. J. Bosch, U. Martin, W. Aperador, J.M. Bastidas, J. Ress, and D.M. Bastidas, Corrosion Behavior of High-Mn Austenitic Fe–Mn–Al–Cr–C Steels in NaCl and NaOH Solutions, *Materials (Basel).*, 2021, **14**(2), p 1–17.

56. J.B. Wang, J.M. Wang, H.B. Shao, J.Q. Zhang, and C.N. Cao, The Corrosion and Electrochemical Behaviour of Pure Aluminium in Alkaline Methanol Solutions, *J. Appl. Electrochem.*, 2007, **37**(6), p 753–758.

57. M.I. Rahim, S. Ullah, and P.P. Mueller, Advances and Challenges of Biodegradable Implant Materials with a Focus on Magnesium-Alloys and Bacterial Infections, *Met. 2018, Vol. 8, Page 532*, Multidisciplinary Digital Publishing Institute, 2018, **8**(7), p 532, doi:10.3390/MET8070532.

58. D. Vojtěch, J. Kubásek, J. Čapek, and I. Pospíšilová, Comparative Mechanical and Corrosion Studies on Magnesium, Zinc and Iron Alloys as Biodegradable Metals, *Mater. Tehnol.*, 2015, **49**(6), p 877–882.

59. R.Y. Pratiwi, A.F. Trinanda, M.W. Ghani Fahmi, S. Astutiningsih, and A. Zakiyuddin, The Effect of Zirconium Addition on Corrosion Behavior of Zn-Zr Alloys as

Biodegradable Orthopedic Implant Application, *IOP Conf. Ser. Mater. Sci. Eng.*, 2020, **833**(1).

60. T. Hryniewicz and K. Rokosz, Corrosion Behaviour of C45 Carbon Steel after Mechanical Surface Finishing, *Metal*, 2004, **20**(5), p 1–8.

61. S. (Jr. . Feliu, Electrochemical Impedance Spectroscopy for the Measurement of the Corrosion Rate of Magnesium Alloys : Brief Review and Challenges, *Metals (Basel).*, 2020, **10**, p 775.

62. M. Corrales-Luna, T. Le Manh, M. Romero-Romo, M. Palomar-Pardavé, and E.M. Arce-Estrada, 1-Ethyl 3-Methylimidazolium Thiocyanate Ionic Liquid as Corrosion Inhibitor of API 5L X52 Steel in H 2 SO 4 and HCl Media, *Corros. Sci.*, Elsevier Ltd, 2019, **153**, p 85–99.

63. S.A. Umoren, M.M. Solomon, and V.S. Saji, Fundamentals of Corrosion Inhibition, *Polymeric Materials in Corrosion Inhibition*, 1st ed., Elsevier, 2022, p 103–127, doi:10.1016/B978-0-12-823854-7.00026-6.

64. F. Witte, N. Hort, C. Vogt, S. Cohen, K.U. Kainer, R. Willumeit, and F. Feyerabend, Degradable Biomaterials Based on Magnesium Corrosion, *Curr. Opin. Solid State Mater. Sci.*, Elsevier, 2008, **12**(5–6), p 63–72.

65. R. Deltombe, K.J. Kubiak, and M. Bigerelle, How to Select the Most Relevant 3D Roughness Parameters of a Surface, *Scanning*, 2014, **36**(1), p 150–160.

66. H. Gerengi, M. Cabrini, M.M. Solomon, and E. Kaya, Assessment of the Corrosion Behaviour of Untreated and Chemically Treated Pure Magnesium in Simulated Body Fluid, *https://doi.org/10.1080/01694243.2022.2095153*, Taylor & Francis, 2022, p 1–17, doi:10.1080/01694243.2022.2095153.

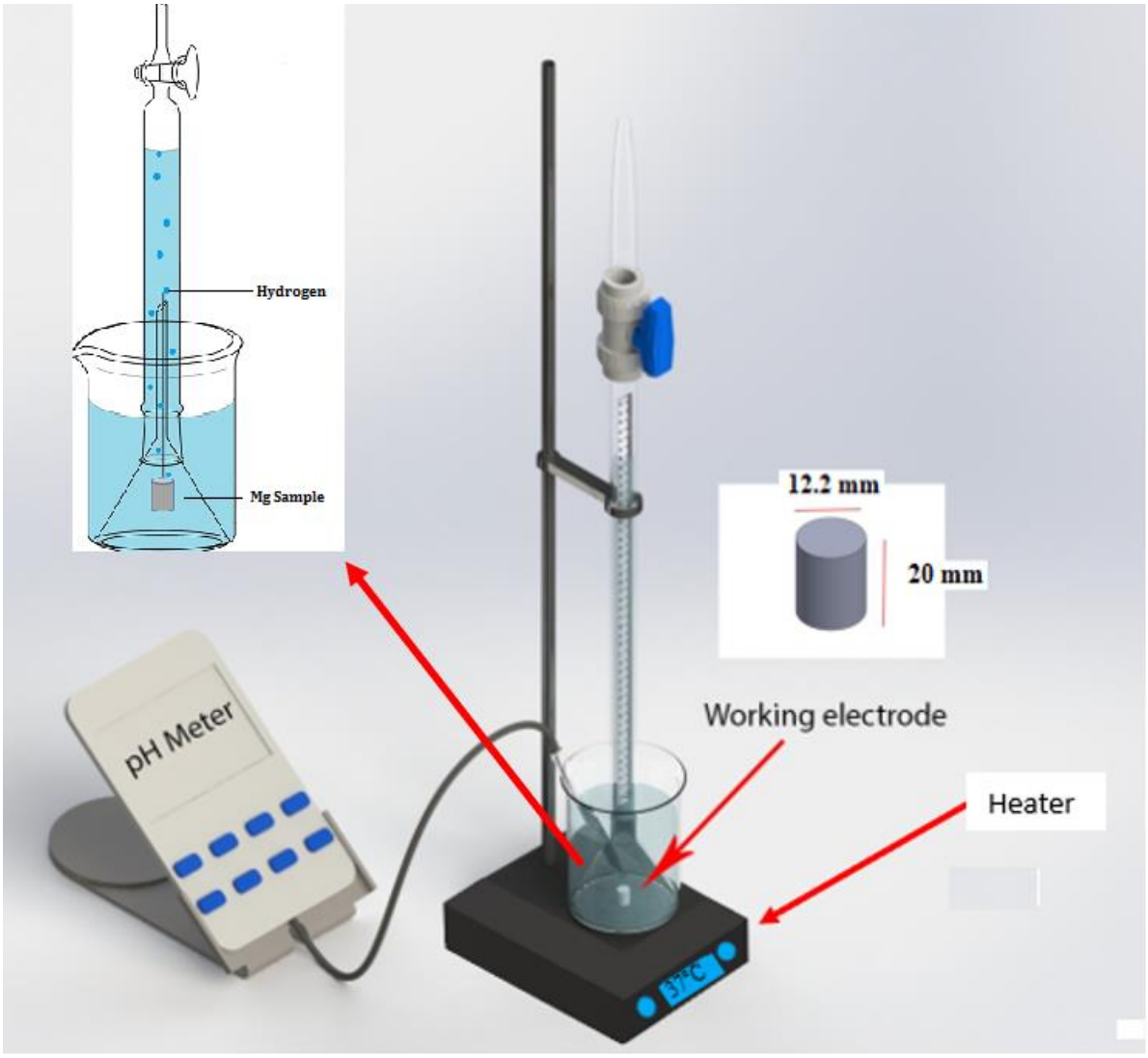

Figure 1: Schematic representation of the volumetric experiments.

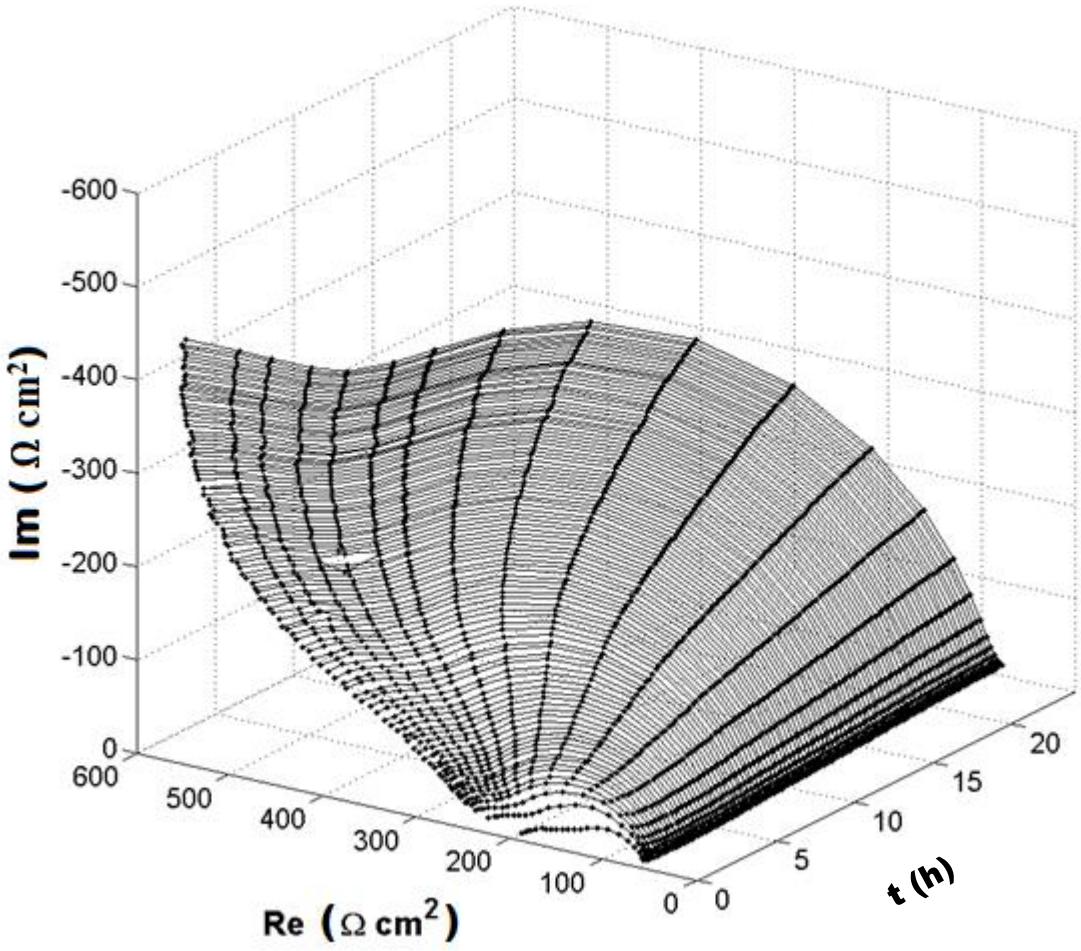

Figure 2: Electrochemical impedance characteristic of WE43B alloy in simulated body fluid at 37 ºC during 24 h of immersion obtained via the Dynamic Electrochemical Impedance Spectroscopy technique.

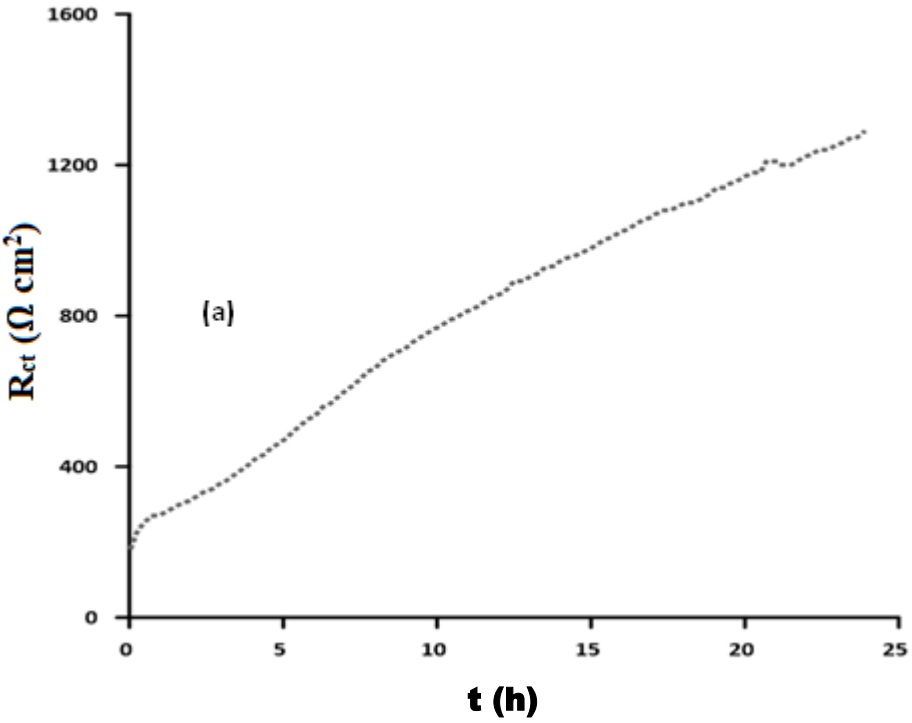
1600
1200
800
400
0
R_{ct} (Ω cm^2)
(a)
0
5
10
15
20
25
t (h)

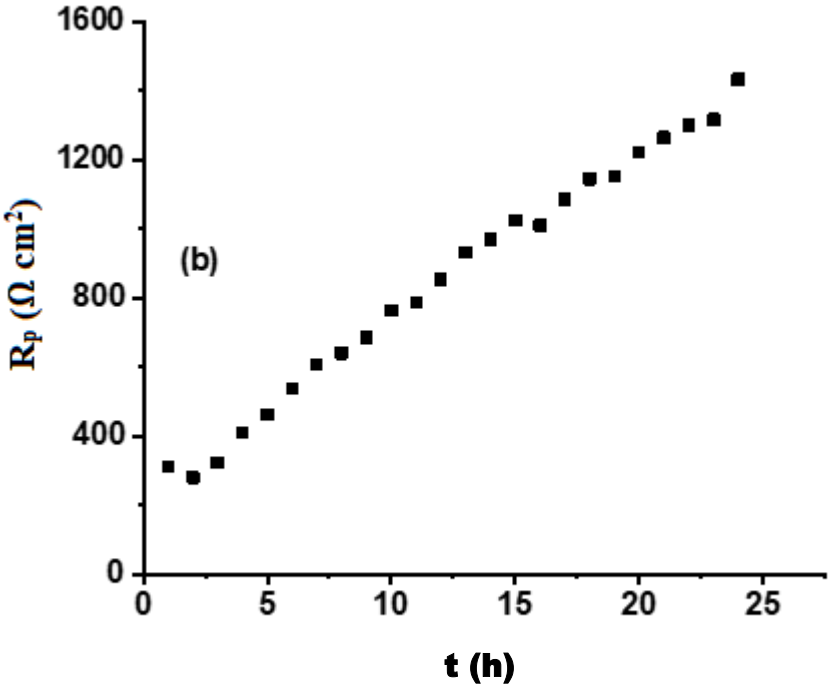
1600
1200
800
400
0
R_p (Ω cm^2)
(b)
0
5
10
15
20
25
t (h)

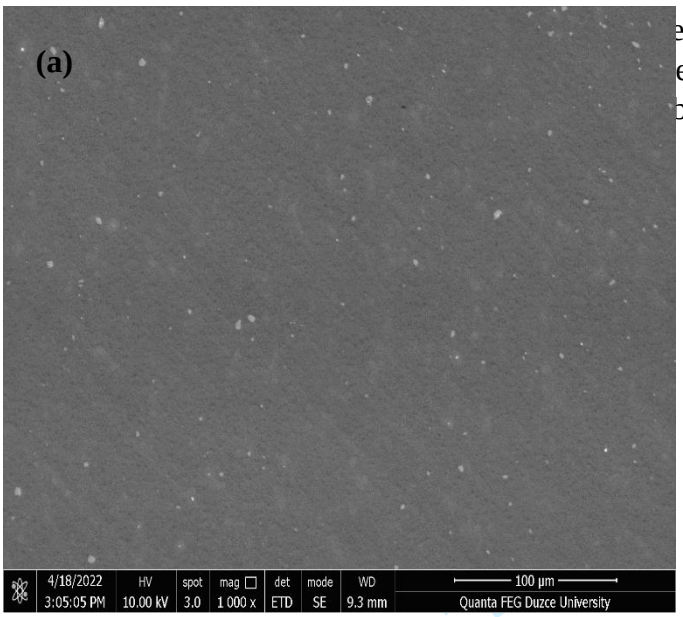
(a)
4/18/2022 3:05:05 PM
HV 10.00 kV
spot 3.0
mag 1 000 x
det ETD
mode SE
WD 9.3 mm
100 µm
Quanta FEG Duze University

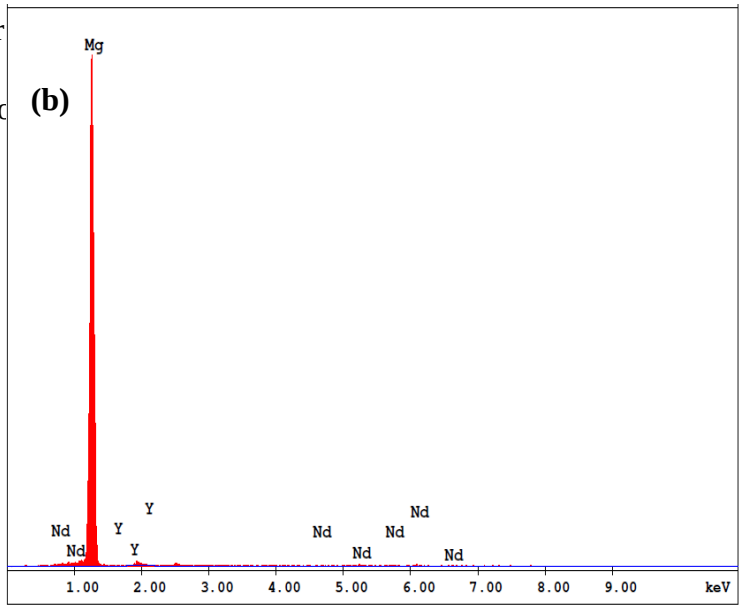
(b)
Mg
Nd
Y
1.00
2.00
3.00
4.00
5.00
6.00
7.00
8.00
9.00
keV

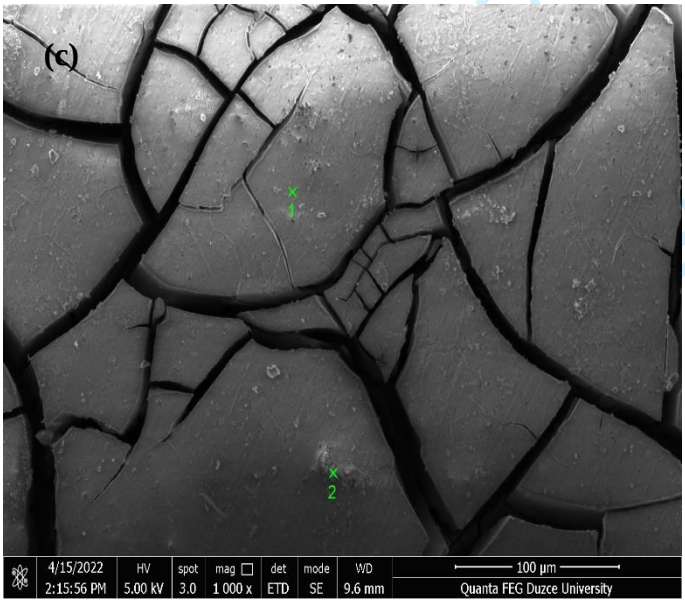
(c)
1
2
4/15/2022 2:15:56 PM
HV 5.00 kV
spot 3.0
mag 1 000 x
det ETD
mode SE
WD 9.6 mm
100 µm
Quanta FEG Duze University

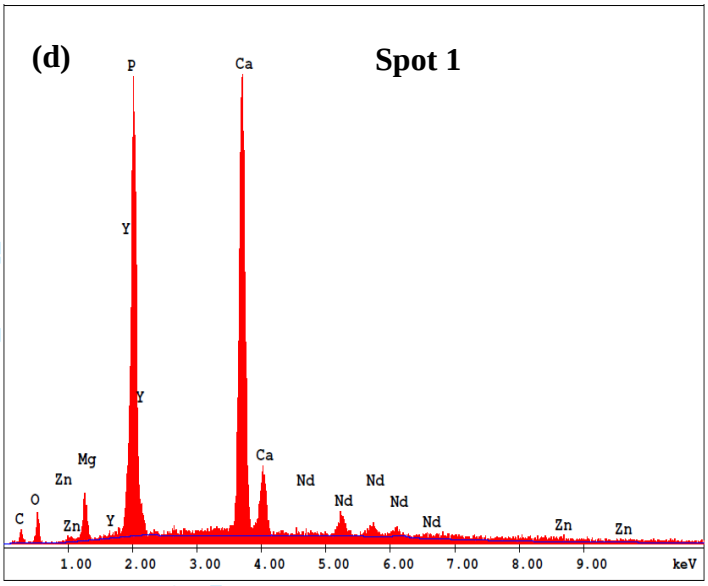
(d)
Spot 1
P
Ca
Y
Mg
Zn
O
C
Nd
1.00
2.00
3.00
4.00
5.00
6.00
7.00
8.00
9.00
keV

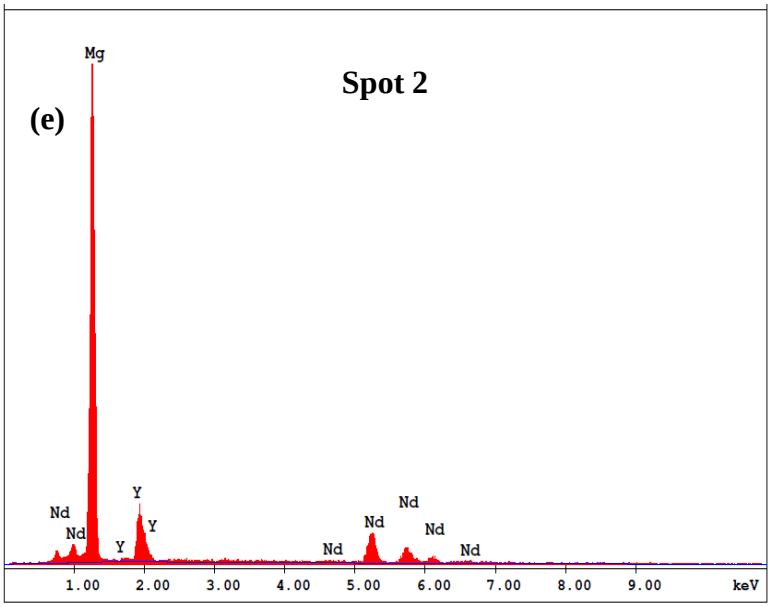
(e)
Spot 2
Mg
Nd
Y
1.00
2.00
3.00
4.00
5.00
6.00
7.00
8.00
9.00
keV

Figure 4: SEM micrographs and EDX spectra of WE43B alloy (a, b) before and (c, d, & e) after corrosion in simulated body fluid at 37 ºC for 24 h.

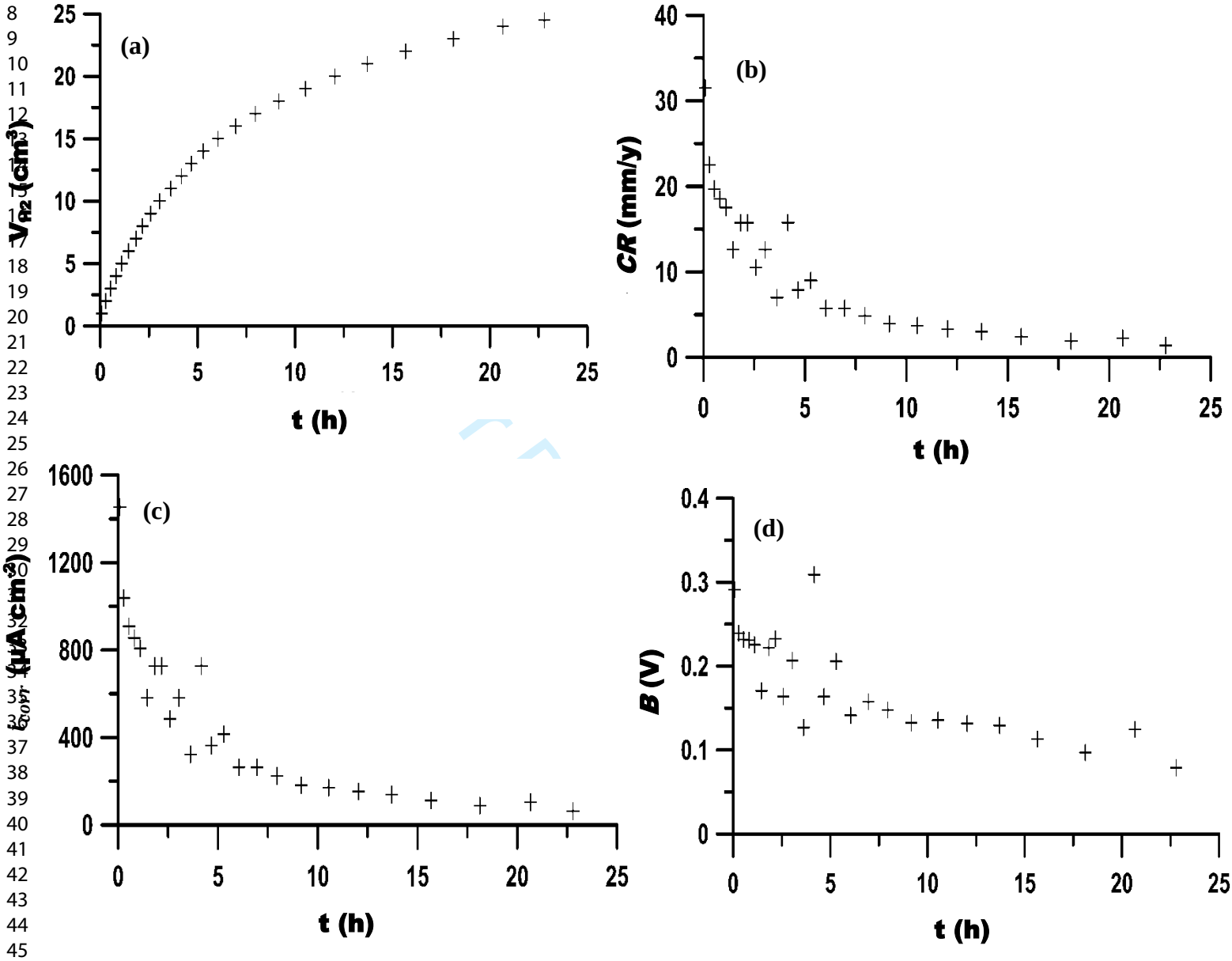

Figure 5: Variation of (a) volume of hydrogen gas evolved, (b) corrosion rate, (c) corrosion current density, and (d) B against time for the corrosion of WE43B alloy in simulated body fluid at 37 ºC.

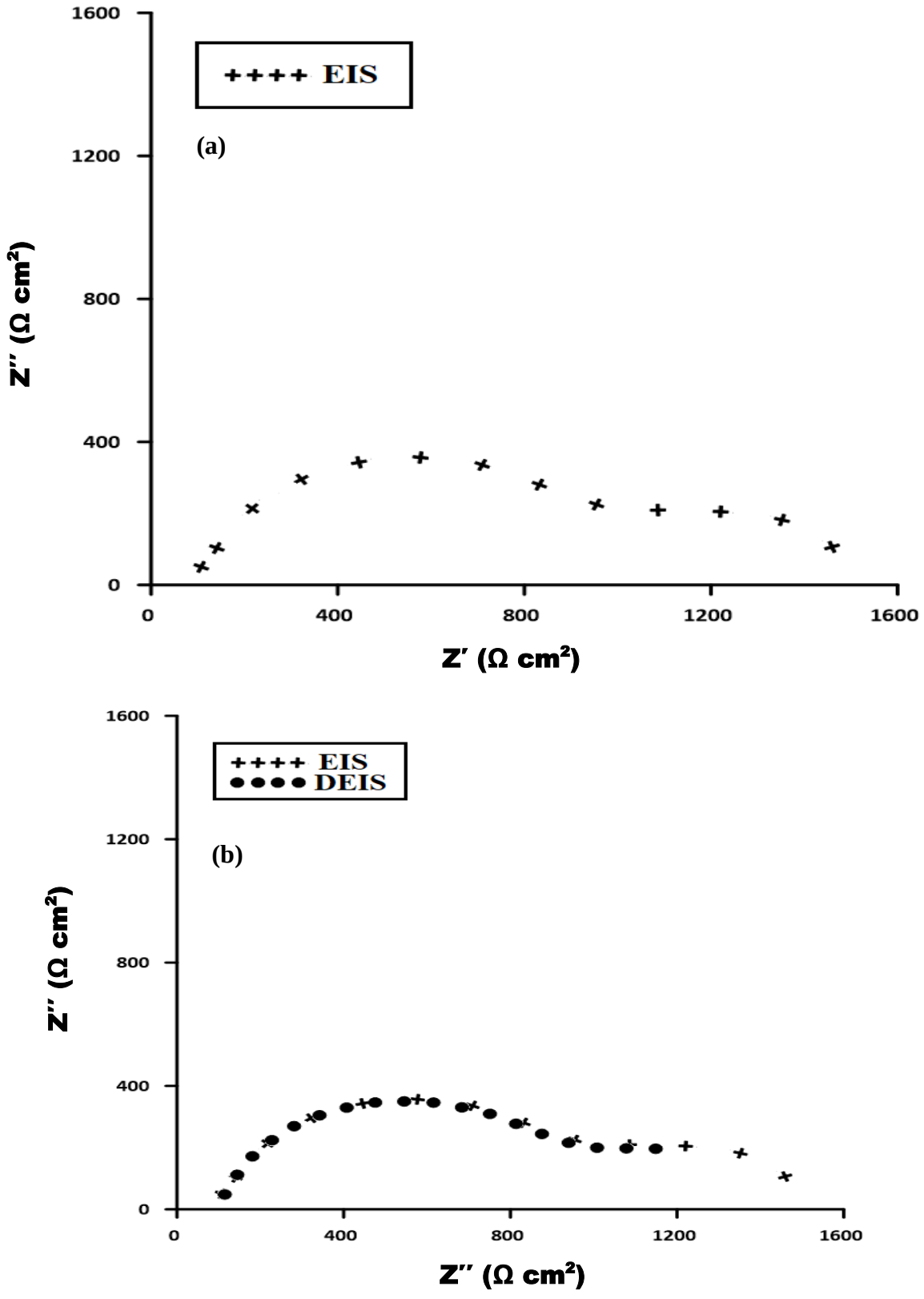

Figure 6: (a) Electrochemical impedance characteristic of WE43B alloy in simulated body fluid at 37 ^{o}C after 24 h of immersion measured using the classical electrochemical impedance spectroscopy technique. (b) Comparison of the Nyquist graphs obtained from the classical EIS and the DEIS.

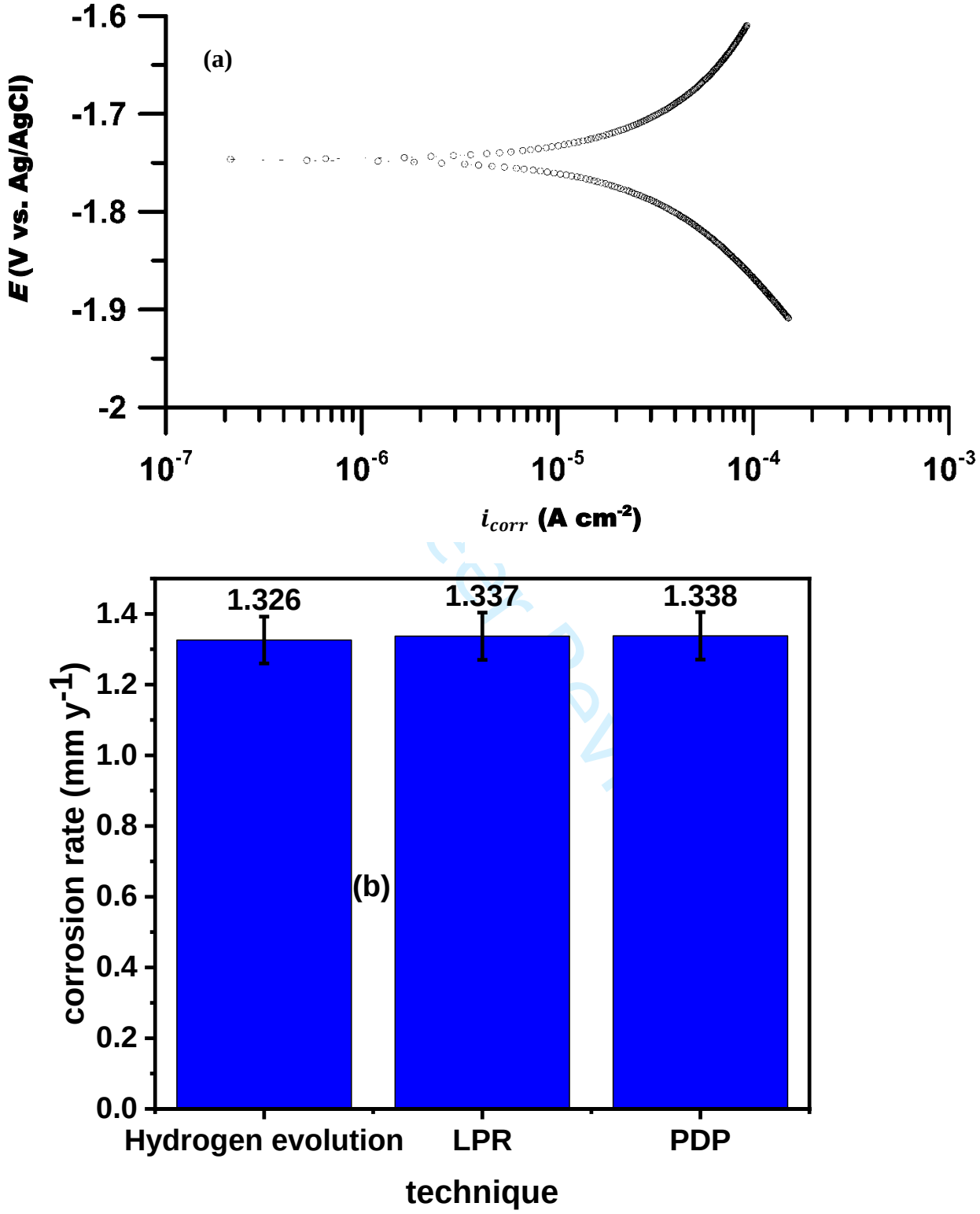

Figure 7: (a) Potentiodynamic polarization curve of WE43B alloy in simulated body fluid at 37 ºC after 24 h of immersion. (b) A comparison of the corrosion rate value obtained from the hydrogen evolution, linear polarization (LPR), and the potentiodynamic polarization (PDP) techniques.

Statistics

Line	Min(nm)	Max(nm)	Mid(nm)	Mean(nm)	Rpv(nm)	Rq(nm)	Ra(nm)	Rz(nm)	Rsk	Rku
Red	-65.114	61.756	-1.679	0.000	126.870	26.053	20.897	94.228	-0.026	2.795
Green	-66.159	84.732	9.286	0.000	150.892	31.590	25.662	121.023	0.082	2.532

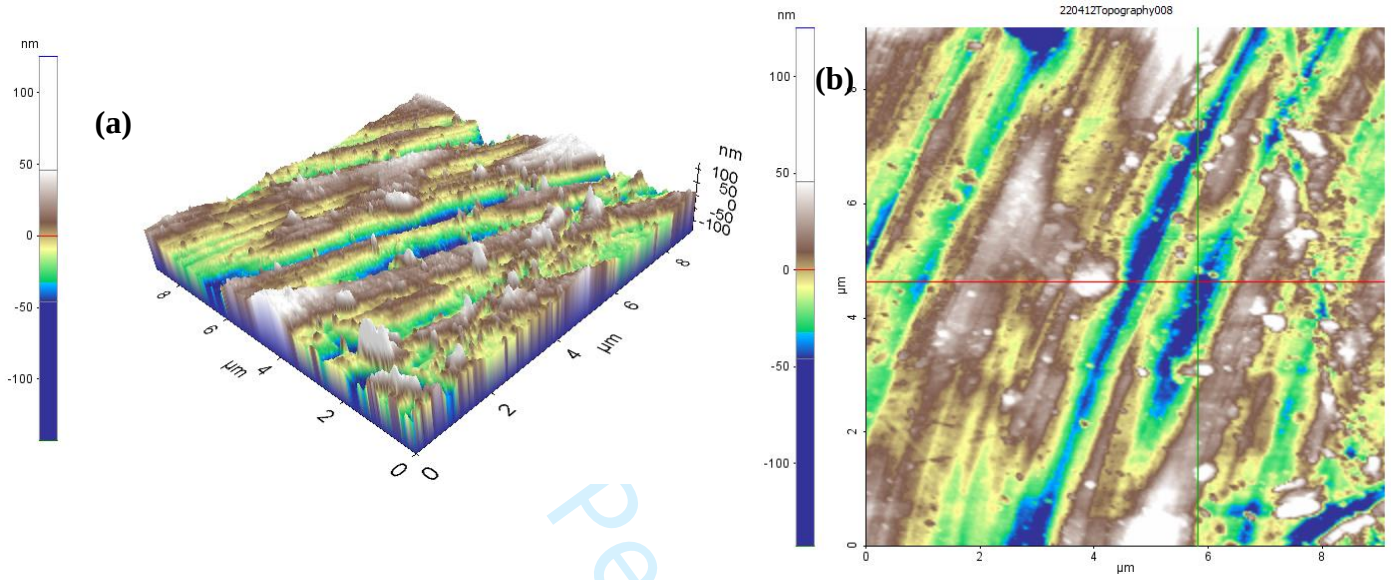

Statistics

Line	Min(nm)	Max(nm)	Mid(nm)	Mean(nm)	Rpv(nm)	Rq(nm)	Ra(nm)	Rz(nm)	Rsk	Rku
Red	-75.528	118.295	21.384	0.000	193.824	36.647	26.410	140.087	-0.283	3.787
Green	-112.594	193.416	40.411	0.000	306.010	51.922	39.241	238.697	-0.749	4.109

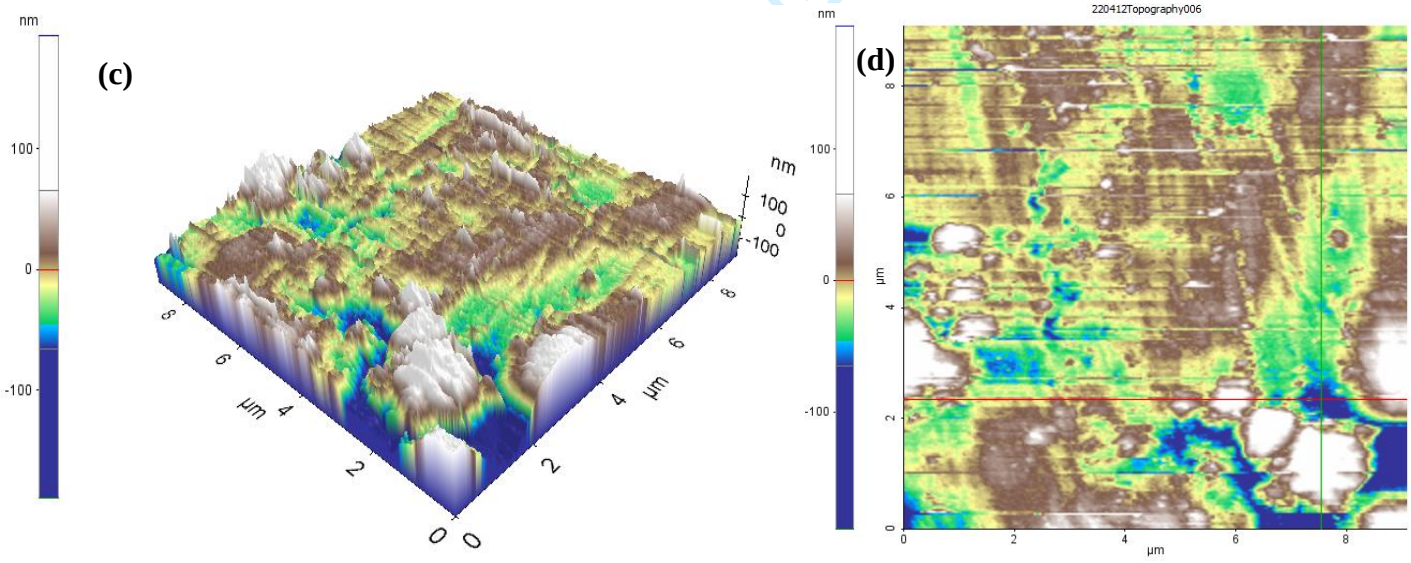

Figure 8: 3D and 2D images of WE43B alloy samples (a, b) before and (c, d) after corrosion in simulated body fluid at 37 ºC for 24 h.